Nanoscale Horizons

Understanding Charge Transfer and Recombination by Interface Engineering for Improving the Efficiency of PbS Quantum Dot Heterojunction Solar Cells

Journal:	*Nanoscale Horizons*
Manuscript ID	NH-COM-02-2018-000030.R1
Article Type:	Communication
Date Submitted by the Author:	13-Mar-2018

Complete List of Authors:	Ding, Chao; The University of Electro-Communications, Faculty of Informatics and Engineering Zhang, Yaohong; The University of Electro-Communications, Liu, Feng; The University of Electro-Communications, Faculty of Informatics and Engineering Kitabatake, Yukiko; Chuo University, Department of Applied Chemistry Hayase, Shuji; Kyushu Institute of Technology, Graduate School of Life Science and Systems Engineering Toyoda, Taro; University of Electro-communications, Engineering Science Wang, Ruixiang; Beijing University of Civil Engineering and Architecture, Beijing Engineering Research Centre of Sustainable Energy and Buildings Yoshino, Kenji; Department of Electrical and Electronic Engineering, Department of Electrical and Electronic Engineering Minemoto, Takashi; Ritsumeikan University, Department of Photonics, Faculty of Science and Engineering Shen, Qing; The University of Electro-Communications, Faculty of Informatics and Engineering

Conceptual Insight statement

For the first time, we demonstrated that in quantum dot heterojunction solar cells (QDHSCs) a spike structure at the interface, i.e., the energy level of the conduction band of the electron transporting layer (ETL) higher than that of the QD absorber, can suppress the charge recombination at the interface. We find that the efficient charge injection can still happen even the spike structure is formed between the QDs absorber and the ETL. We think this is because that the shallow defect states in the ETLs can serve as additional pathway to transport the photoexcited electrons from the QDs to the electron collecting electrode (FTO). By taking advantage of these characteristics, we can greatly improve the efficiency of the QDHSCs just by slightly tunning the conduction band energy offset between the ETL and the QDs. In addition, by probing free electron absorption in FTO using broadband transient absorption spectroscopy, we find that the ultra-fast electron transfer occurs in a time scale of a few hundred femtoseconds from PbS QDs to FTO through the $Zn_{1-x}Mg_xO$ compact layer. We believe our findings would provide a guidance for enhancing the photovoltaic performance of QD-based solar cells further.

Journal Name

ARTICLE

Understanding Charge Transfer and Recombination by Interface Engineering for Improving the Efficiency of PbS Quantum Dot Heterojunction Solar Cells

Received 00th January 20xx,
Accepted 00th January 20xx

DOI: 10.1039/x0xx00000x

www.rsc.org/

Chao Ding, [a,h] *Yaohong Zhang,* [a] *Feng Liu,* [a] *Yukiko Kitabatake,* [b] *Shuzi Hayase,* [*c,g] *Taro Toyoda,* [a,g] *Ruixiang Wang,* [d] *Kenji Yoshino,* [*e,g] *Takashi Minemoto,* [*f,g] *Qing Shen*[*a,g]

In quantum dot heterojunction solar cells (QDHSCs), the QD active layer absorbs sunlight and then transfers the photogenerated electrons to an electron-transport layer (ETL). It is generally believed that the conduction band minimum (CBM) of the ETL should be lower than that of the QDs to enable efficient charge transfer from the QDs to the collection electrode (here, FTO) through the ETL. However, by employing Mg-doped ZnO ($Zn_{1-x}Mg_xO$) as a model ETL in PbS QDHSCs, we found that an ETL with a lower CBM is not necessary to realize efficient charge transfer in QDHSCs. The existence of shallow defect states in the $Zn_{1-x}Mg_xO$ ETL can serve as additional charge-transfer pathways. In addition, the conduction band offset (CBO) between the ETL and the QD absorber was, for the first time, revealed to significantly affect interfacial recombination in QDHSCs. We demonstrate that a spike in the band structure at the ETL/QD interface is useful for suppressing interfacial recombination and improving the open-circuit voltage. By varying the Mg doping level in ZnO, we were able to tune the CBM, defect distribution and carrier concentration in the ETL, which play key roles in charge transfer, recombination and therefore the device performance. PbS QDHSCs based on the optimized $Zn_{1-x}Mg_xO$ ETL exhibited a high power conversion efficiency of 10.6%. Our findings provide important guidance for enhancing the photovoltaic performance of QD-based solar cells.

Introduction

Over the past decades, quantum dot solar cells (QDSCs) have been widely studied as a promising next-generation photovoltaic technology to generate clean and renewable energy. Among the various kinds of QDSCs, PbS QDSCs have attracted much attention due to their significant advantages such as ease of solution processing, high stability, and potential multiple exciton generation.[1-4] In addition, the band gap of PbS QDs can be readily tuned over a wide range (0.5-1.6 eV) by adjusting their particle size due to the quantum confinement effect, which enables a wide spectral response from the ultraviolet to the near-infrared region.[5] Due to these unique properties, QDSCs based on PbS QDs have achieved impressive device performance, with a power conversion efficiency (PCE) exceeding 11%.[6]

Colloidal PbS QDs are often employed in depleted-heterojunction solar cells, which contain five different parts: a transparent conducting oxide (TCO) layer (e.g., fluorine-doped tin oxide (FTO) and indium-doped tin oxide (ITO)), an electron-transport layer (ETL) (or hole-blocking layer (HBL), e.g., ZnO, SnO_2, and TiO_2), PbS QDs, a hole-transport layer (HTL) (or electron-blocking layer (EBL), e.g., MoO_x and organic small molecules), and contact electrodes (e.g., Au and Ag).[7-11] Unlike perovskite solar cells, which can still function without the inclusion of a HTL or ETL, in PbS QD heterojunction solar cells (QDHSCs), both an ETL and a HTL are necessary for achieving high efficiency, because they enhance charge extraction and suppress charge recombination at the TCO/QD and QD/gold interfaces.[12-14, 15] This may result because QDs have more surface defects than perovskites, which can cause severe back recombination of injected electron carriers at the FTO/QD interface (Figure S1, Supporting Information).

[a] *Faculty of Informatics and Engineering, The University of Electro-Communications, 1-5-1 Chofugaoka, Chofu, Tokyo 182-8585, Japan.*
[b] *Department of Applied Chemistry, Chuo University, 1-13-27, Kasuga, Bunkyo, Tokyo 112-8551, Japan.*
[c] *Graduate School of Life Science and Systems Engineering, Kyushu Institute of Technology, 2-4 Hibikino, Wakamatsu-ku, Kitakyushu, Fukuoka 808-0196, Japan.*
[d] *Beijing Engineering Research Centre of Sustainable Energy and Buildings, Beijing University of Civil Engineering and Architecture, No.15 Yongyuan Road, Huangcun, Daxing, Beijing 102616, China.*
[e] *Department of Electrical and Electronic Engineering, Miyazaki University, 1-1 Gakuen Kibanadai Nishi, Miyazaki 889-2192, Japan.*
[f] *Department of Photonics, Faculty of Science and Engineering, Ritsumeikan University, 1-1-1 Noji Higashi, Kusatsu, Siga 525-8577, Japan.*
[g] *CREST, Japan Science and Technology Agency (JST), 4-1-8 Honcho, Kawaguchi, Saitama 332-0012, Japan.*
[h] *China Scholarship Council, Level 13, Building A3, No.9 Che gong zhuang Avenue, Beijing 100044, China.*

In a QDHSC, the p-type layer is a QD film, and the n-type layer is an ETL that accepts photogenerated electron carriers. The built-in electric field is mainly distributed near the ETL/QD interface.[11, 16] Usually, when a favourable cliff-like conduction band structure forms at the ETL/QD interface (i.e., the conduction band of the QDs is higher than that of the ETL), electron injection will occur. When the conduction band of the QDs is lower than that of the ETL, forming a spike structure, electron injection will be retarded.[13, 16] Such observations have been demonstrated in QD-sensitized solar cells and Cu(In,Ga)Se_2 (CIGS) solar cells.[13, 17-19] However, in this work, we found that in magnesium (Mg)-doped ZnO/PbS QDHSCs, the ZnO layer does not need to have a lower conduction band energy to realize efficient charge transfer, that is, although a spike structure is formed between the QDs and the "*electron acceptor*", charge injection can still occur, and improved injection of photogenerated electrons can occur at a certain conduction band offset (CBO). Here, we used a thin Mg-doped ZnO film (~30 nm) ($Zn_{1-x}Mg_xO$, x=0, 0.05, 0.10, 0.15, 0.20) as an ETL with tuneable characteristics. In fact, $Zn_{1-x}Mg_xO$ films with high transparency and tuneable band gaps have been employed in PbX (X=S, Se) QDHSCs as a novel electron-transport material, and greatly improved solar cell efficiencies have been obtained with enhanced open-circuit voltage (V_{oc}).[8, 20, 21] However, previous studies did not provide further insight into the role of Mg doping, for example, its impact on the carrier dynamics, including charge injection and recombination. Here, we explored the carrier injection and recombination mechanism in FTO/$Zn_{1-x}Mg_xO$/PbS QDHSCs by varying the Mg doping level in ZnO. The effect of Mg doping on the intrinsic properties (e.g., defect states and carrier concentration) of the $Zn_{1-x}Mg_xO$ layer and the ensuing device performance were systematically studied by several spectral measurements, such as transient photovoltage (TPV) decay measurement and ultrafast transient absorption (TA) spectroscopy. Interestingly, we found that Mg doping can greatly alter the photophysical properties of ZnO and, in particular, that the resulting spike band structure of $Zn_{1-x}Mg_xO$/PbS QDs can inhibit charge recombination, while the shallow defect states can serve as additional pathways to transport photoexcited electrons from the QDs to the electron-collecting electrode. More importantly, we also revealed the time constant of this transport process by TA measurement.

Results and discussion

The $Zn_{1-x}Mg_xO$ ETL was prepared using a sol-gel method as described previously.[22, 23] Briefly, the Zn-Mg mixed sol-gel solution was prepared by mixing zinc salt (Zn^{2+}) and magnesium salt (Mg^{2+}) (0%, 5%, 10%, 15% and 20% molar percentage based on metal ions), and then, the mixed sol-gel solution was spin-coated onto pre-cleaned FTO substrates and sintered at 290℃. A ZnO film without Mg doping was prepared as a reference.[23] X-ray photoelectron spectroscopy was carried out to verify the Mg doping. The binding energy (BE) scale was calibrated with the C 1s peak of carbon at 284.28 eV. Figure 1 shows the XPS spectra of the $Zn_{1-x}Mg_xO$ (x=0, 0.05, 0.10, 0.15, 0.20) films with different Mg doping levels. Typical BE peaks at 1021.3 and 1044.5 eV, assigned to Zn^{2+} $2P_{3/2}$ and $2P_{1/2}$, are observed in all $Zn_{1-x}Mg_xO$ spectra, as shown in Figure 1 (a), confirming the presence of divalent Zn ions in all samples.[24] As shown in Figure 1 (b), the BE peak assigned to Mg 2p is observed at 49.7 eV in the $Zn_{1-x}Mg_xO$ (x=0.5, 0.10, 0.15) spectra, while that of the x=0.2 film is observed at 48.7 eV with enhanced intensity and area, which suggests that increased Mg doping in $Zn_{1-x}Mg_xO$ can lead to the formation of MgO for x≥0.2. Figure 1 (c) shows BE components at 532.4 eV and 533.9 eV in the $Zn_{1-x}Mg_xO$ spectra, attributable to the O^{2-} ions in Zn-O or Mg-O and the oxygen-deficient components of the films, respectively.[25-27] The XPS results confirm the successful doping of Mg in the ZnO films.[28, 29]

The optical absorption spectra of the $Zn_{1-x}Mg_xO$-coated FTO samples, shown in Figure 2 (a), indicate a continuous blueshift

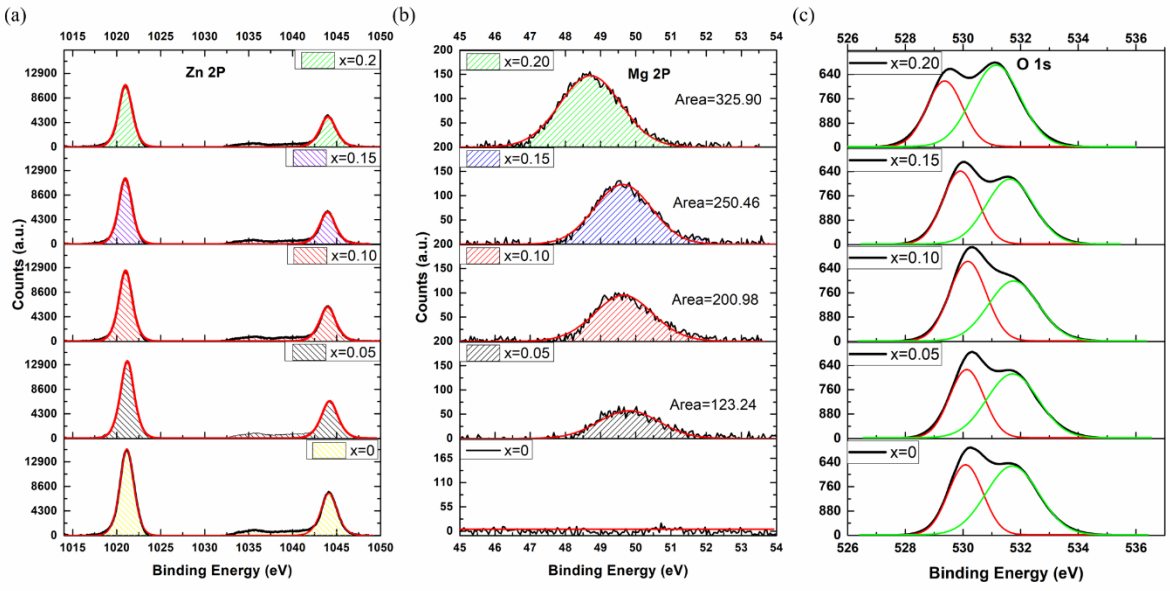

Figure 1. XPS spectra of the $Zn_{1-x}MgxO$ films (x=0, 0.05, 0.10, 0.15, 0.20): (a) Zn 2p, (b) Mg 2p, and (c) O 1s with two resolved O bonding (red and black lines) components.

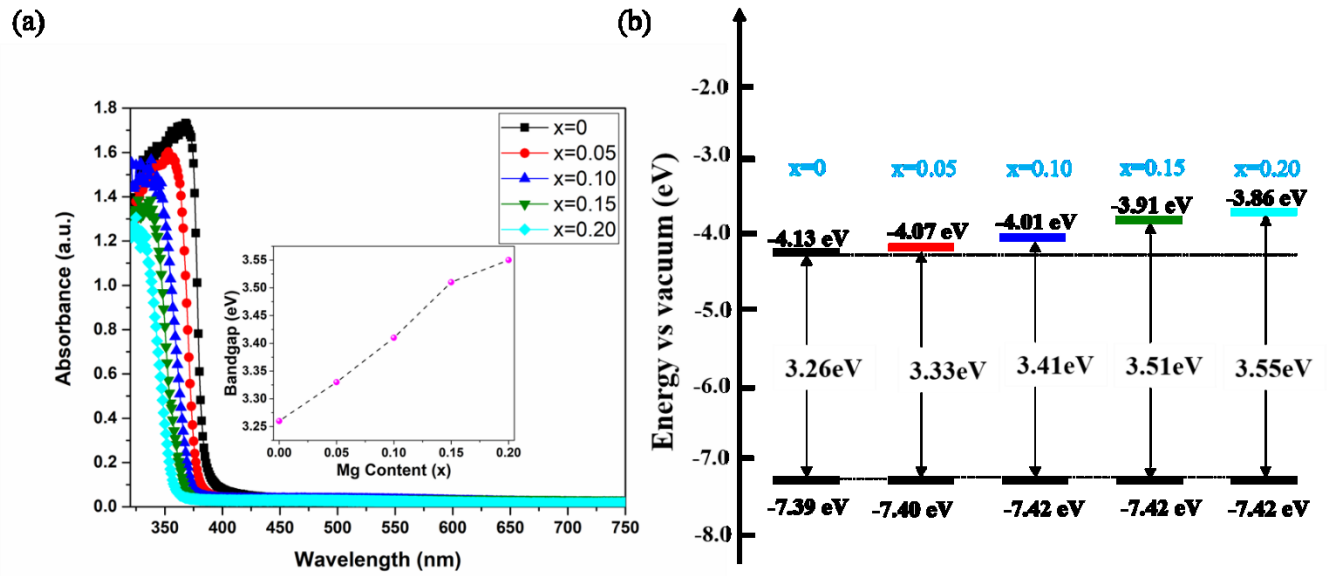

Figure 2. (a) Optical absorption spectra of the $Zn_{1-x}Mg_xO$ films. The inset shows an increase in the bandgap of $Zn_{1-x}MgxO$ films with Mg doping. (b) Experimentally determined diagram of energy levels (relative to the vacuum level) of the $Zn_{1-x}Mg_xO$ films (x=0-0.20), the valence band maximum (VBM) and the conduction band minimum (CBM) are represented in eV.

of the absorption edges with increasing Mg content (x=0-0.2). The optical band gaps, *E*g, obtained by linearly extrapolating the Tauc plot $[(\alpha h\nu)^2$ vs. photon energy$]$[30], are presented in the inset of Figure 2 (a), and the corresponding band gap of the $Zn_{1-x}Mg_xO$ films continuously increases from 3.26 to 3.56 eV with Mg doping, which is in agreement with previous reports.[8, 29] According to other reports of $Zn_{1-x}Mg_xO$,[28, 31] the suitable doping of Mg^{2+} at Zn^{2+} sites in ZnO induces an obvious change in the conduction band (CB) energy of the ternary oxide, but the influence on the valence band (VB) edge of $Zn_{1-x}Mg_xO$ is negligible. To verify these results, the VB edge energy levels of the five $Zn_{1-x}Mg_xO$ samples were measured by photoelectron yield spectroscopy (PYS), as shown in Figure S2. The VB edge energy levels were obtained from the intersection of the baseline and the tangent to the spectra, and we also found a negligible effect of Mg doping on the VB edge energy levels of the $Zn_{1-x}Mg_xO$ films. The energy band diagram of the $Zn_{1-x}Mg_xO$ films is schematically depicted in Figure 2 (b) by combining the above results of both the band gap and the VB edge level. The energy band diagram of the $Zn_{1-x}Mg_xO$ films is schematically depicted in Figure 2 (b) by combining the above results of both the band gap and the VB edge level. From this energy band diagram, a continuous shift in the conduction band minimum (CBM) towards higher energy with increasing Mg doping is observed. The general trend of these values is good agreement with previous reports.[8, 32]

Our above characterization suggests that ZnO films can be doped with Mg by a facile sol-gel method and the band gaps can be easily tuned by adjusting the Mg doping level. Next, we used $Zn_{1-x}Mg_xO$ (x=0, 0.05, 0.10, 0.15, 0.20) thin films (~30 nm) to prepare PbS QDHSCs. PbS QDs were synthesized using a modified hot-injection method,[33] and QDs of different sizes were prepared by controlling the injection temperature. The excitonic peak of the PbS QDs was located at 1.19 eV, as shown in Figure S3 (a), and the VB edge energy level of the PbS QDs was confirmed to be -5.24 eV by PYS measurement, as shown in Figure S3 (b). By combining the results of both bandgap and VB edge level, the CB edge level was determined to be -4.05 eV, as

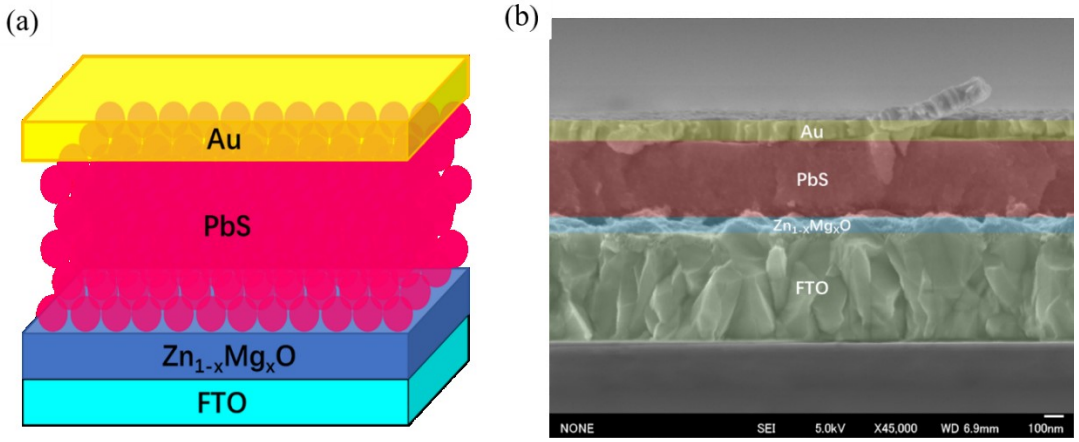

Figure 3. (a) Schematic illustration of $Zn_{1-x}Mg_xO$/PbS solar cell structure. (b) Cross-sectional SEM image of a typical $Zn_{1-x}Mg_xO$/PbS solar cell (~300 nm thick PbS QD active layer).

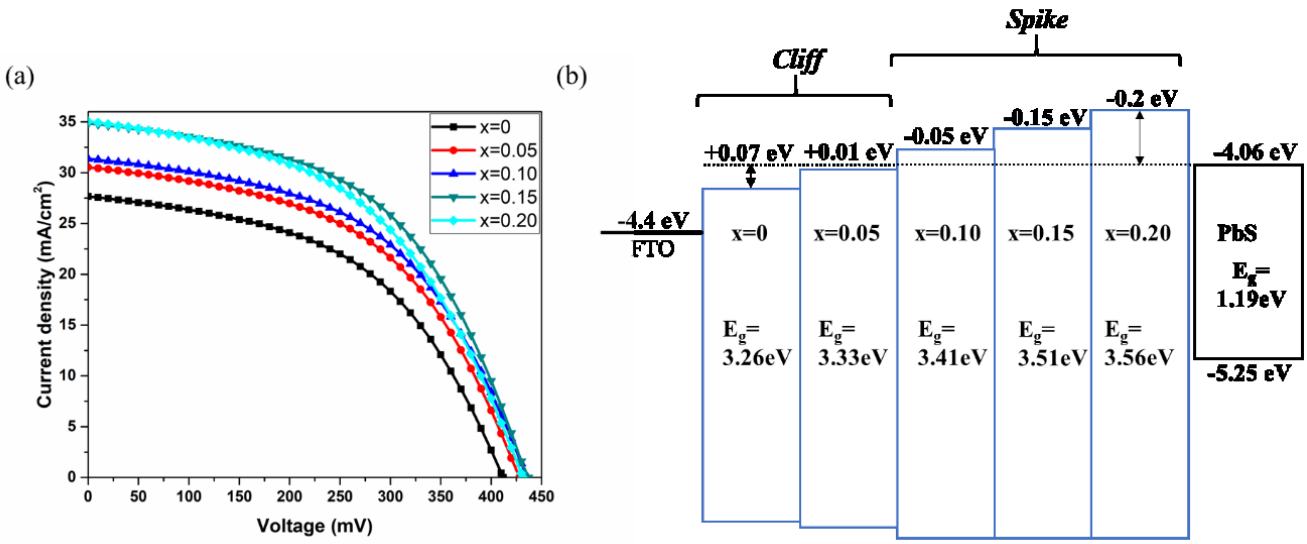

Figure 4. (a) J-V characteristics of PbS QDHSCs with $Zn_{1-x}Mg_xO$ (x=0~0.20) under simulated AM 1.5G illumination. (b) Band alignment of PbS QDs and $Zn_{1-x}Mg_xO$ with different Mg contents (x=0~0.2).

Table 1. Statistical averages of the photovoltaic performance parameters of 24 devices for each type of the QDHSCs [a].

Sample	J_{sc} (mA/cm²)	V_{oc} (mV)	FF (%)	R_s (Ω.cm²)	R_{sh} (Ω.cm²)	PCE (%)
x=0	26.34±0.75 (27.64)	419.06±5.8 (412)	49.94±0.85 (49.3)	64.33±3.02 (67.35)	99.86±2.97 (102.83)	5.51±0.11 (5.62)
x=0.05	29.33±0.88 (30.53)	434.18±6.35 (428)	50.53±1.52 (49.9)	55.66±4.78 (60.44)	204.93±4.23 (209.16)	6.43±0.08 (6.51)
x=0.10	30.91±1.27 (31.36)	437.53 ±4.19 (436)	51.05±1.21 (50.3)	52.33±3.71 (48.92)	220.27±3.14 (223.41)	6.79±0.09 (6.88)
x=0.15	33.59±1.32 (34.86)	437.62±6.95 (437)	51.82±1.55 (51.1)	43.52±2.96 (40.56)	174.03±3.99 (178.02)	7.55±0.21 (7.76)
x=0.20	34.23±0.93 (35.05)	434.12±6.05 (434)	47.18±1.55 (48.3)	59.33±4.11 (57.75)	74.17±3.67 (78.44)	7.01±0.34 (7.35)

[a] Results for the device with highest PCE are shown in parentheses.

seen in the inset of Figure S3 (b). The corresponding transmission electron microscope (TEM) image reveals that the average size of the PbS QDs is approximately 3.5 nm (Figure S4 (a)), and the high-resolution transmission electron microscopy (HR-TEM) image shows that the PbS QDs exhibit a high-crystalline structure with interplanar distances of 0.342 and 0.291 nm, corresponding to the (111) and (200) planes of rock-salt PbS, respectively (Figure S4 (b)).The crystallinity of PbS QD is further supported by the selected area electron diffraction (SAED) pattern (see insets in Figure S4 (b)). Figures 3 (a) and (b) show the typical schematic structure and a cross-sectional scanning electron microscopy (SEM) image, respectively, of a $Zn_{1-x}Mg_xO$/PbS solar cell, wherein the PbS QD layer (300 nm) serves as the light absorbing layer.

Figure 4 (a) shows the typical photocurrent density–voltage (J–V) characteristics of the five types of QDHSCs upon standard 100 mW cm^{-2} AM1.5G illumination. We measured 24 devices for each type of QDHSC. The average values of photovoltaic parameters such as open-circuit voltage (V_{oc}), short-circuit current (J_{sc}), fill factor (FF), series resistance (R_s), shunt resistance (R_{sh}), and PCE are summarized in Table 1. Compared with the undoped device (ZnO), the $Zn_{1-x}Mg_xO$ films significantly improved the device performance. As expected, the V_{oc} was continuously enhanced with increasing Mg doping level due to the reduced loss of electrons, as observed in other reports.[8, 20] We consider the enhanced V_{oc} to result from the higher CBM of $Zn_{1-x}Mg_xO$, which is shown in Figure 4 (b). However, when the Mg doping level exceeds 10%, the V_{oc} becomes saturated due to dominant charge recombination at the $Zn_{1-x}Mg_xO$/QD interface caused by the high level of Mg doping, as demonstrated previously.[32, 34, 35] Surprisingly, the J_{sc} of the device continued to increase at high Mg doping level. For example, the J_{sc} of the device with a 15% Mg doping level was greatly improved by 30%. The control photovoltaic device based on pure ZnO showed a PCE of 5.51 ± 0.11%, with a smaller V_{oc} of 419.06 ± 5.8 mV and a lower FF of 49.94 ± 0.85%. The solar cell based on the optimized Mg doping level achieved the highest efficiency of 7.55 ± 0.21%, with a V_{oc} of 437.62 ± 6.95 mV, J_{sc} of 33.59 ± 1.32 mA/cm² and FF of 51.82± 1.55%, as

shown in Table 1, providing an improvement in efficiency of over 36% compared to the ZnO control devices.

To elucidate the difference in the photovoltaic performance when changing the Mg doping level in ZnO, we first investigated the band alignment between the PbS and $Zn_{1-x}Mg_xO$ layers. As shown in Figure 4 (b), the CBO values between the PbS QDs (Eg=1.19 eV) and $Zn_{1-x}Mg_xO$ were controlled from +0.07 eV to -0.2 eV by changing the Mg doping level in ZnO. When the Mg doping level was below 10%, the CB of $Zn_{1-x}Mg_xO$ was lower than that of the PbS QDs, i.e., the CBO was positive, thus forming a cliff structure; when the Mg doping amount was above 10%, the conduction band of $Zn_{1-x}Mg_xO$ was higher than that of the PbS QDs, i.e., the CBO was negative, thus forming a spike structure. Generally, the larger the conduction band offset of the cliff structure (CBO_{cliff}), the better the injection of the photogenerated electrons will be. However, when the ETL/QD interface forms a spike structure (CBO_{spike}), the injection of photogenerated electrons is retarded.[13, 16, 20] However, in our case, a large CBO_{spike} in a certain range instead led to better electron injection and an enhanced J_{sc}, which may be related to the presence of shallow defect states in the $Zn_{1-x}Mg_xO$ films and the decreased carrier concentration due to Mg doping, which will be discussed further below.

To investigate the effect of Mg doping on the solar cell performance, the room-temperature photoluminescence (PL) was measured. Figure 5 (a) shows the PL spectra of the $Zn_{1-x}Mg_xO$ samples at room temperature. The PL spectrum of the ZnO film was fit by a Gaussian function, as shown in Figure S5 (a), which gives five peaks centred at 380, 400, 478, 529, and 572 nm. The narrow ultraviolet emission at 380 nm is related to the near band edge transition in ZnO. Furthermore, the edge of this near band edge-related emission shows a continuous shift towards shorter wavelength with increasing doping level, which reflects the band gap broadening due to Mg doping and is consistent with the results of the optical absorption spectra in Figure 2 (a). The emission regions of 400~600 nm are attributed to shallow and deep level defects (as shown in Figure S5 (b)) within the ZnO crystal, such as interstitials and vacancies of zinc and oxygen.[36] In general, the violet (400 nm) and blue (470 nm) emission in the PL spectra of ZnO are related to shallow defects, while the green (529 nm) and yellow (572 nm) emission are related to deep defects.[37] Therefore, the PL spectra can be divided into sections I, II, and III, representing band, shallow and deep defect-dominated emission, respectively.

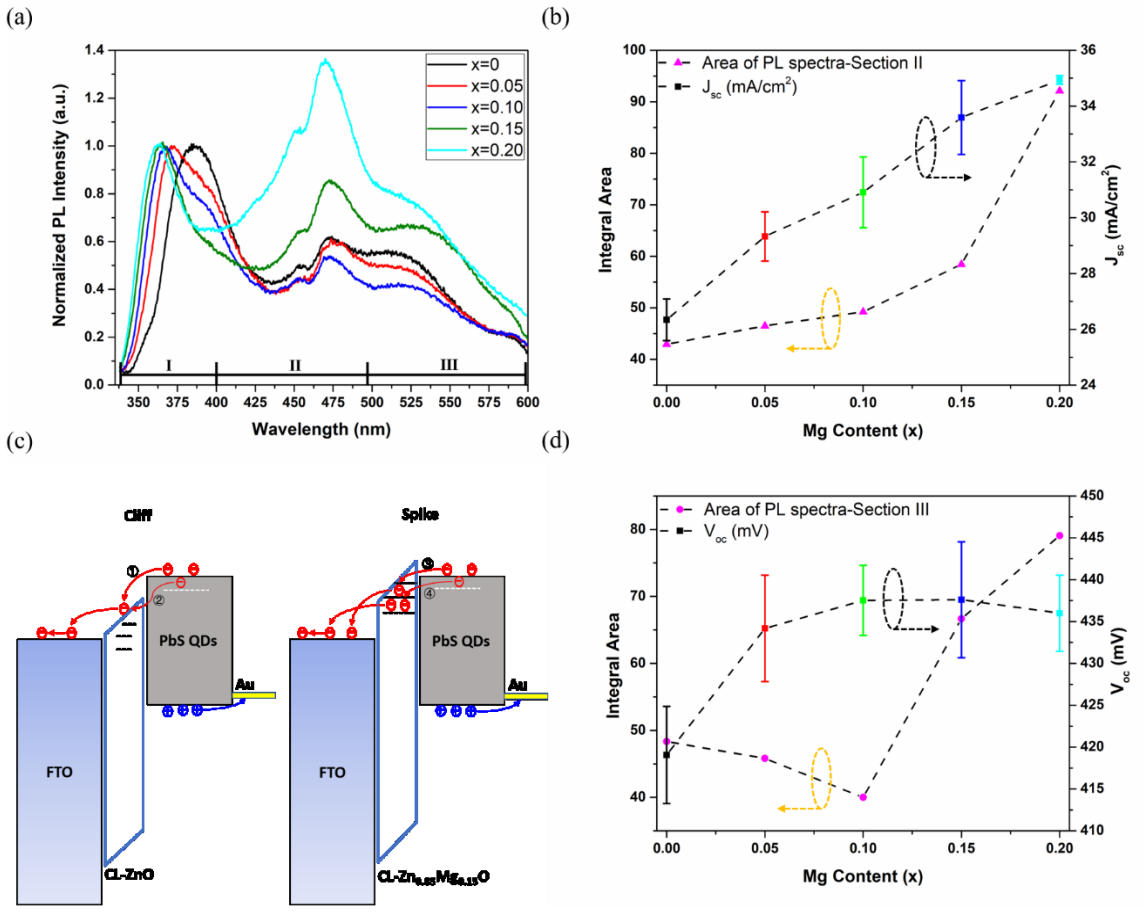

Figure 5. (a) Room temperature PL spectra of $Zn_{1-x}Mg_xO$ films (x=0, 0.05, 0.10, 0.15 and 0.20). (b)The integral area of section II range of PL spectra of $Zn_{1-x}Mg_xO$ films and J_{sc} of $Zn_{1-x}Mg_xO$/PbS QDHSCs. (c) Carrier-injection processes for photogenerated electrons (red arrows) and holes (blue arrow) in $Zn_{1-x}Mg_xO$/PbS QDHSCs (cliff and spike structure) under short circuit condition. ① Photogenerated electrons can be injected from the QDs CB to the $Zn_{1-x}Mg_xO$ CB; ②Captured photo-generated carriers can be injected from QDs intragap state to the $Zn_{1-x}Mg_xO$ CB; ③ Photogenerated electrons can be injected from the QDs CB to the $Zn_{1-x}Mg_xO$ shallow defects; ④ Captured photo-generated carriers can be injected from QD intragap state to the $Zn_{1-x}Mg_xO$ shallow defects. (d) The integral area of section III range of PL spectra of $Zn_{1-x}Mg_xO$ films and V_{oc} of $Zn_{1-x}Mg_xO$/PbS QDHSCs.

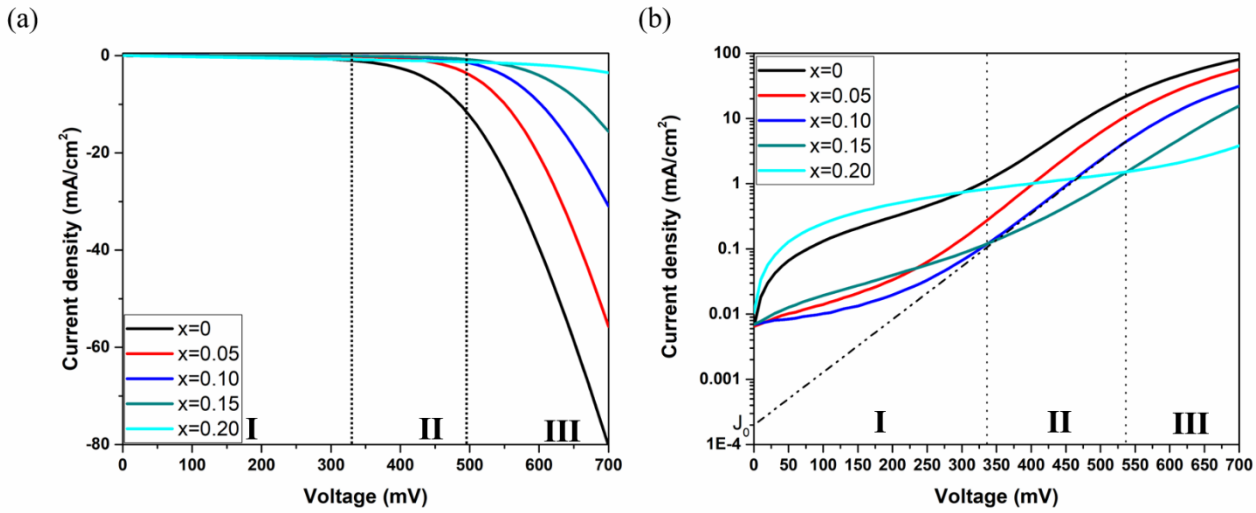

Figure 6. (a) Typical *J-V* characteristics of PbS QDHSCs with $Zn_{1-x}Mg_xO$ (x=0~0.20) ETLs measured under dark. (b) Semilog plot of *J-V* curves measured under dark and using the absolute values of current density. The three regions indicate three different effects in the solar cell: Region I accounts for leakage (shunt) currents, Region II accounts for recombination currents, and Region III accounts for series resistance.

Table 2. Diode ideality factor (n) and reverse saturation current density (J_0) of the PbS QDHSCs with $Zn_{1-x}Mg_xO$ (x=0~0.20).

Sample	*n*	J_0
X=0	1.73	7.374E-3
X=0.05	1.39	3.867E-4
X=0.10	1.35	1.974E-4
X=0.15	1.82	1.865E-3
X=0.20	2.54	3.727E-2

Figure 5 (b) shows the integral area of the shallow defect-related emission range in the PL spectra (i.e., section II). It is well known that the integrated area of the PL emission from defect states is proportional to the defect state density of the corresponding energy level. Interestingly, we found that the change in the integral area for section II (shallow defect state emission) with Mg doping level was in good accordance with the change in J_{sc}, suggesting that the electron-transfer process may have some relation with the shallow defect states. This can be understood by the fact that in the absence of external excitation, charge-carrier transfer from low to high energy levels is difficult. In addition, although the thickness of $Zn_{1-x}Mg_xO$ is low (~30 nm), it is not low enough for electrons to transport directly from the QDs to FTO by tunnelling. Therefore, when a spike band structure is formed, the shallow defect states in the $Zn_{1-x}Mg_xO$ layer may act as additional pathways for charge carriers to transfer from the QDs to the FTO electrode. As shown in Figure 5 (c), in our PbS QDHSCs, when $Zn_{1-x}Mg_xO$ and the PbS QDs form a *cliff* band structure, the photogenerated electrons can be transferred from the QD CB to the $Zn_{1-x}Mg_xO$ CB by pathways ① and ② (intragap states). When $Zn_{1-x}Mg_xO$ and the PbS QDs form a *spike* band structure, transfer of the photogenerated carriers to $Zn_{1-x}Mg_xO$ through pathways ① and ② is difficult due to the energy barrier. However, due to the favourable energy level alignment between the shallow defect level of $Zn_{1-x}Mg_xO$ and the CB or intragap states of the PbS QDs, photogenerated electrons can be injected into $Zn_{1-x}Mg_xO$ through pathways ③ and ④ and then collected at the FTO electrode. In addition, the charge injection rate from the absorber to the ETL depends on the density of accepting states (i.e., sub-band-gap surface states) in the ETL.[38-41] The Mg-doped ZnO ETL provides a greater density of accepting states for electron injection due to the lower carrier concentration in $Zn_{1-x}Mg_xO$ (~10^{14} cm^{-3}), as shown in Figure S6. The broadened optical band gap of Mg-doped ZnO enhances the light absorption of the PbS QD layer, which also improves the J_{sc}.

Notably, the properties of the ETL also have a significant effect on charge recombination in the device. Figure 5 (d) shows that as the Mg doping level increased, the integral area of section III (deep defect state emission) first decreased from x=0 to 0.10 and then increased from x=0.10 to 0.20, suggesting that with an increase in the Mg doping level, the deep defects caused by oxygen vacancies in $Zn_{1-x}Mg_xO$ gradually decrease, but when the Mg doping level exceeds 10%, the excessive Mg

doping may introduce new deep defects in ZnO, e.g., $Mg_{Interstitial}$ (as seen in Figure S5 (b)), which can easily become carrier recombination centres,[37] leading to greater charge recombination at the $Zn_{1-x}Mg_xO$/PbS QD interface. This also explains the saturated V_{oc} observed under excessive Mg doping conditions, as shown in Figure 5 (d). However, our *J-V* results show that when the Mg doping level exceeds 10%, the V_{oc} tends to decrease to a saturated value rather than continuously decrease, possibly because the formed *spike* band structure alleviates interfacial recombination to a certain extent, as demonstrated in other types of heterojunction solar cells.[19, 32, 35] Therefore, the change in V_{oc} with increased Mg doping level in our QDHSCs is considered to be a combined effect of defect states in $Zn_{1-x}Mg_xO$ and the formed CBO.

To gain further insight into the effect of Mg doping in $Zn_{1-x}Mg_xO$ on charge recombination in the solar cells, the diode performance of the solar cells was studied by examining the dark *J-V* characteristics. As seen in Figure 6 (a), the dark current of the PbS QDHSCs decreased with increasing Mg doping level. The continuous decrease in the dark current of the solar cells may be due to the increased built-in potential in the $Zn_{1-x}Mg_xO$ layer, attributed to the increased Femi level of Mg-doped ZnO.[41] To better understand the effect of Mg doping on device performance, we next analysed the diode behaviour of our devices in the dark by introducing the traditional equivalent circuit model (Figure S7).[42] In this model, the *J-V* behaviour of the solar cell includes four constituent parts: a photocurrent source, a diode, a series resistor, and a shunt resistor. This model can be mathematically represented by the following equation:[43]

$$\mathbf{J} = \boldsymbol{J_0}\left[\boldsymbol{exp}\left(\frac{\boldsymbol{q(V-JR_s)}}{\boldsymbol{nk_BT}}\right) - \mathbf{1}\right] + \frac{\boldsymbol{V-JR_S}}{\boldsymbol{R_{sh}}} - \boldsymbol{J_{ph}} \qquad (1)$$

where J_0 is the reverse bias saturation current density, q is the elementary charge, R_s is the series resistance, n is the diode ideality factor, k_B is Boltzmann's constant, T is the temperature, and R_{sh} is the shunt resistance. Figure 6 (b) shows the dark curves derived from Figure 6 (a) using the semi-log scale, which can be divided into regions I, II, and III, corresponding to the three parts of eq. (1), which describe how the different components of the solar cell equivalent circuit (Figure S6) affect the *J-V* response of the cell at different voltages. At low voltages (region I: the 3rd term in eq. (1)), the *J-V* curve is mainly related to R_{sh} (shunt current); at intermediate voltages (region II: the 1st term in eq. (2)), the *J-V* curve is related to diode parameters J_0 and n (recombination current); while at high voltages (region III: the 2ed term in eq. (1)), the *J-V* curve is determined by R_s.[43] These regions provide important information when evaluating the *J-V* response curve. For instance, a steep slope in region III generally indicates a low R_s.[43] Thus, according to the observation of the dark current density in regions I, II and III in Figure 6 (b), we found that the changes in R_{sh} and R_s of the devices with increasing Mg doping level are in agreement with the R_{sh} and R_s measured from *J-V* characterization under illumination (Table 1). When the Mg doping level was increased from 0 to 10%, the current leakage (region I) of the device continuously decreased, but when the Mg doping level was above 20%, significant current leakage was observed. This could be attributed to the fact that the appropriate Mg doping level (x=0.1) leads to better crystallization of the ZnO film and further decreases the defects and current leakage of the thin films.[44]

The values of n and J_0 of the PbS QDHSCs with $Zn_{1-x}Mg_xO$ were determined by least-squares fitting the dark *J-V* curves in section II to eq. (1), and the values are summarized in Table 2.[45] The n value is related to the recombination mechanism in the solar cell. When n is close to 1, direct recombination (band-to-band) dominates; otherwise, indirect recombination mechanisms, such as interfacial recombination and trap-assisted recombination (n=2), dominate.[9] Our results show that the changes in the n value of the five different devices are consistent with the changes in the density of deep defects in $Zn_{1-x}Mg_xO$ with increasing Mg doping level (as shown in Figure 5 (d)). The decrease in the ideality factor from 1.73 (x=0) to 1.35 (x=0.10) with the increase in Mg doping level in ZnO indicates that the contribution of indirect recombination (back-transfer recombination of the injected electrons through trapping by deep defects in $Zn_{1-x}Mg_xO$) is relatively reduced under open-circuit conditions due to removal of the $Zn_{1-x}Mg_xO$ deep trap sites. When the Mg doping level was above 10%, with an increase in deep level defects in $Zn_{1-x}Mg_xO$, the n value increased rapidly to become larger than that of the undoped device of 1.73. Although $Zn_{1-x}Mg_xO$ and PbS QDs will form a spike band structure when the Mg doping level is above 10%, this does not lead to reduced indirect recombination of the charges. Previously, the Greenham group reported that reducing the ZnO carrier concentration by nitrogen doping can prevent interfacial recombination in CQDSCs;[41] however, our results show that interfacial recombination is not suppressed despite the much lower carrier concentration of the Mg-doped devices compared with the undoped device (as shown in Figure S6). These results indicate that indirect recombination of charges in the PbS QDHSCs strongly depends on the deep level defect density in $Zn_{1-x}Mg_xO$. In addition, the J_0 values displayed a similar trend for the device doped with 10% Mg, showing the smallest J_0 value and the lowest charge recombination.

For detailed analysis, the effect of increased Mg doping on the recombination mechanism in $Zn_{1-x}Mg_xO$/PbS QDHSCs was examined by transient photovoltage (TPV) decay analysis. When a PbS QDHSC is illuminated by a laser pulse under open-circuit conditions, an open-circuit photovoltage is generated across the full device. When the incident laser is switched off, all photogenerated carriers recombine, and the photovoltage decays.[9, 46-48] Figure 7 (a) shows the TPV decay curves of the solar cells with increasing Mg doping level in ZnO. All decay curves were well fitted by a three-exponential-function equation, and the corresponding parameters are summarized in Table 3. The three-component fitting implies that three recombination processes are present in this case,[9] similar to our previously reported results.[9, 46-48] First, the ultrafast process (< 0.1 ms, constant τ_1 in Table 3, in the high-V_{oc} regime) can be related to intrinsic trapping-assisted recombination in PbS and the $Zn_{1-x}Mg_xO$ films. In Table 3, the decay time constant τ_1 was almost the same (approximately 0.02 ms) for all devices, considering the ultrafast time scale and fitting uncertainty. Notably, the weight of A_1 decreases from the x=0 device to the x=0.1 device, this change reflects the reduction in the trap state

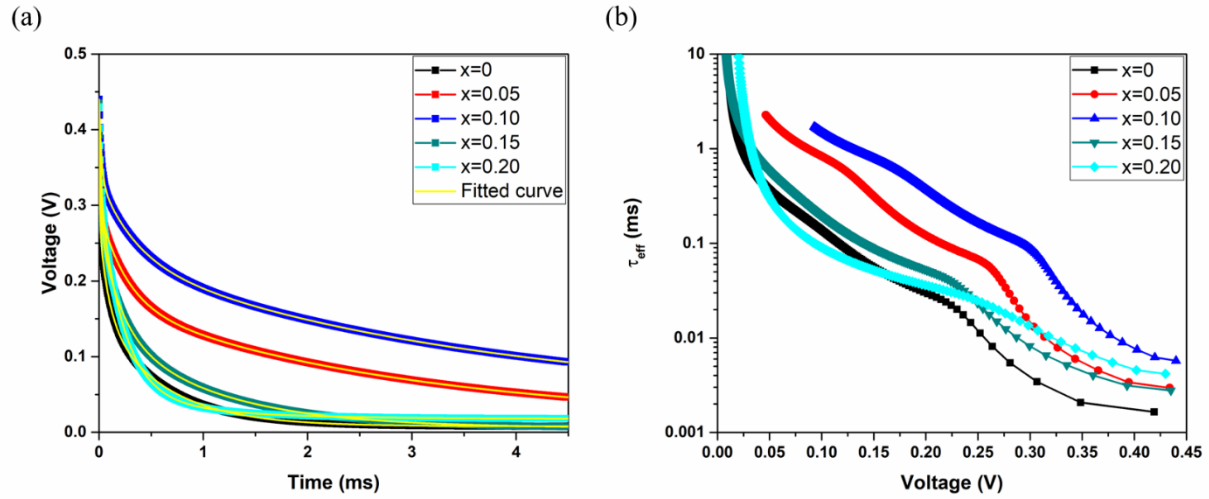

Figure 7. (a) Open-circuit photovoltage decay curves for $Zn_{1-x}Mg_xO$/M-PbS QDHSCs, showing three dominant decay processes. (b) The effective carrier lifetimes calculated from the voltage decay curves for $Zn_{1-x}Mg_xO$/M-PbS QDHSCs.

Table 3. Time constants and weight obtained by fitting the open-circuit photovoltage decay curves of the PbS QDHSCs with a three-exponential function as shown in the table.

Sample	$V_{oc} = A_1e^{-t/\tau_1} + A_2e^{-t/\tau_2} + A_3e^{-t/\tau_3}$					
	A_1 ($A_1/(A_1+A_2+A_3)$)	τ_1 (ms)	A_2 ($A_1/(A_1+A_2+A_3)$)	τ_2 (ms)	A_3 ($A_1/(A_1+A_2+A_3)$)	τ_3 (ms)
X=0	0.440 (47.5%)	0.023±0.0006	0.426 (46.0%)	0.285±0.004	0.060 (6.5%)	2.275±0.004
X=0.05	0.323 (32.4%)	0.015±0.001	0.294 (29.5%)	0.408±0.001	0.381 (38.1%)	3.46±0.01
X=0.10	0.243 (24.3%)	0.025±0.0005	0.259 (26.0%)	0.411±0.003	0.495 (49.7%)	5.17±0.03
X=0.15	0.381 (38.4%)	0.019±0.0005	0.366 (36.9%)	0.273±0.005	0.245 (24.7%)	1.438±0.006
X=0.20	0.269 (27.1%)	0.023±0.001	0.658 (66.2%)	0.256±0.001	0.067 (6.7%)	8.166 ±0.005

density of the $Zn_{1-x}Mg_xO$ films and thus reduced recombination through trap states. For the second process (i.e., in the medium-V_{oc} regime), the related constant τ_2 is more than 0.2 ms, and this process can be related to interfacial recombination at the $Zn_{1-x}Mg_xO$/PbS interface. Table 3 shows that the trends in the values of A_2 and the decay time constant τ_2 are in good agreement with the trend of deep level defect intensity (Figure 5 (d)) in $Zn_{1-x}Mg_xO$ with increasing Mg doping. This indicates that a reduction in the $Zn_{1-x}Mg_xO$ deep level defect density can mitigate interfacial recombination between electrons trapped in the $Zn_{1-x}Mg_xO$ layers and holes in the VB (or intragap states near the VB) of the PbS QDs. In the third decay process (i.e., in the low-V_{oc} regime), V_{oc} disappears completely. This process represents the direct recombination of electrons in the CB of FTO and holes in the VB of the PbS layer, and the related decay time constant τ_3 is on the order of a few ms. The weights of A_3 and τ_3 significantly increased for $Zn_{0.9}Mg_{0.1}O$. We found that solar cells based on $Zn_{0.8}Mg_{0.2}O$ have the longest recombination lifetime (τ_3) in process 3, probably due to the larger CBO (0.2 eV) between $Zn_{0.8}Mg_{0.2}O$ and the PbS QDs, which forms an energy barrier that slows the direct recombination of free electrons and holes. The effective carrier lifetimes (τ_{eff}) were determined from the TPV decay curves using the defined equations (see details in the SI). As shown in Figure 7 (b), the dependence of the effective carrier lifetime on the photovoltage can also be divided into three sections, corresponding to the three photovoltage decay processes. Throughout the V_{oc} regime, the τ_{eff} values of the $Zn_{0.9}Mg_{0.1}O$-based device were 2~3 times higher than those of the other devices and were in the order of 10% > 5% > 0% > 15% > 20% Mg doping, which can be understood through the above discussions. Although the $Zn_{0.9}Mg_{0.1}O$-based cell showed the longest recombination lifetime, the $Zn_{0.85}Mg_{0.15}O$-based solar cell had the largest V_{oc} and the fastest V_{oc} decay. This indicates that the recombination of photogenerated carriers in the device is related to both factors, i.e., deep level defects in $Zn_{1-x}Mg_xO$ and the formed CBO.

For the above-studied PbS QDs (denoted "M-PbS", E_g=1.19 eV), the effect of the CBO on suppressing the interfacial recombination of the charge carriers is not obvious, which we attribute to the relatively small value of the CBO between $Zn_{1-x}Mg_xO$ and the QDs. Thus, large-sized PbS QDs (denoted "L-PbS") were prepared to increase the CBO between $Zn_{1-x}Mg_xO$ and the PbS QDs. Figure S8 (a) shows the first exciton

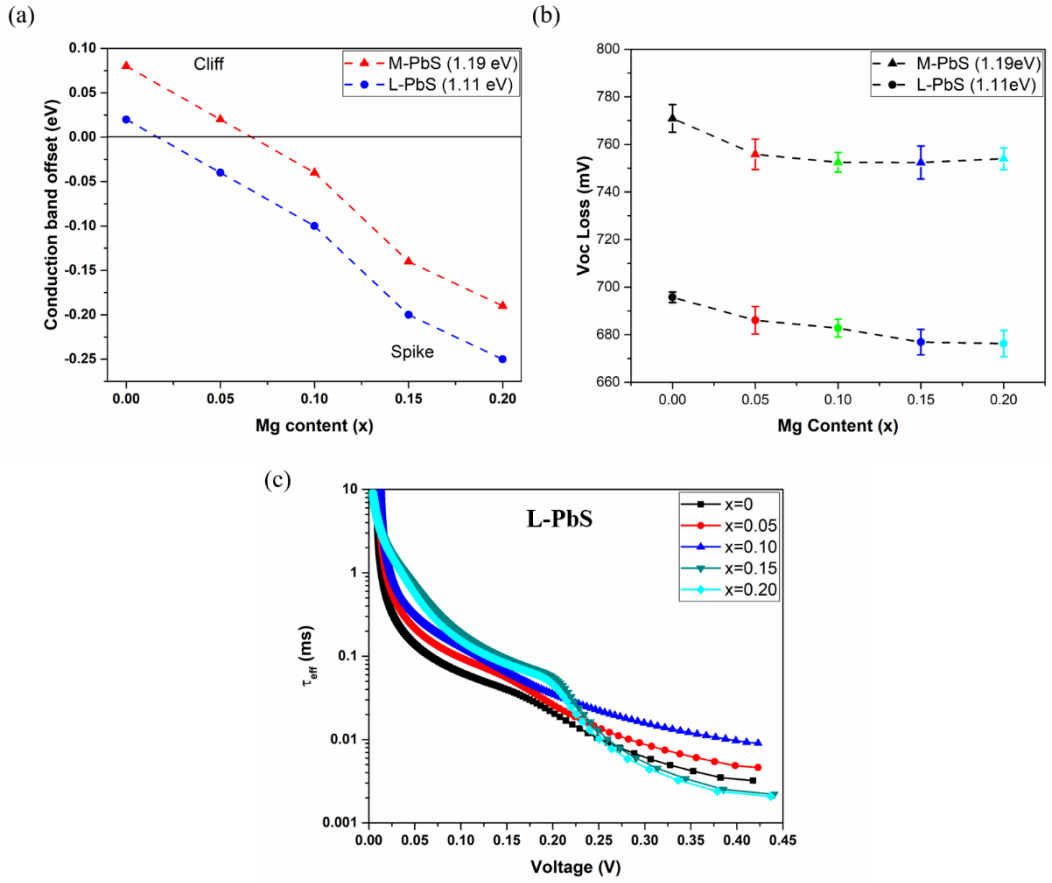

Figure 8. (a) The conduction band offset values for both PbS QDs (i.e., M-PbS:1.19 eV and L-PbS:1.11 eV) with $Zn_{1-x}Mg_xO$, respectively. (b)The Voc loss of both M-PbS QDHSCs and L-QDHSCs, respectively. (c) The effective carrier lifetimes calculated from the voltage decay curves for $Zn_{1-x}Mg_xO$/L-PbS QDHSCs.

absorption peak of the L-PbS QDs, located at 1.11 eV. The VB edge energy level of the L-PbS QDs was confirmed to be -5.22 eV by PYS measurement, as shown in Figure S8 (b). By combining the results of both the band gap and the VB edge level, the CB edge level was determined to be -4.11 eV (inset of Figure S8 (b)). The TEM and HRTEM images shows that the average size of the L-PbS QDs was approximately 3.9 nm and the QDs were highly crystalline (Figure S9). The photovoltaic parameters of the QDHSCs based on L-PbS are summarized in Figure S10. Figure 8 (a) shows both the *cliff* and *spike* band structures of the CBO in the PbS QDHSCs. The CBO values between the L-PbS QDs and $Zn_{1-x}Mg_xO$ were controlled from +0.10 eV to -0.25 eV by changing the Mg doping level in ZnO. In the QDHSCs, the V_{oc} loss strongly depended on charge recombination, which was mainly affected by the junction characteristics.[49] The V_{oc} loss of all devices is shown in Figure 8 (b). The V_{oc} loss was defined as $E_g/q - V_{oc}$, where q is the elementary charge. Compared with the effect of $Zn_{1-x}Mg_xO$, the influence of the change in the size of the QDs on the V_{oc} loss is more obvious. With an increase in QD size, the PL lifetime of the QDs increased from 276 ns to 985 ns, as shown in Figure S11. The increase in the PL lifetime is believed to mainly result from the reduction of surface defects in the PbS QDs. In addition, compared with the smaller PbS QDs, the defect states are mainly distributed near the CBM in the large-sized QDs.[50] Therefore, devices based on larger QDs showed less V_{oc} loss. We found that V_{oc} loss in the L-PbS QDs-based devices decreases with increasing deep defect density in $Zn_{1-x}Mg_xO$ when the Mg doping content is above 10%. We suggest this is because the positive effect of the larger CBO_{spike} value on carrier recombination is greater than the negative effect of deep defects in $Zn_{1-x}Mg_xO$. We also measured the effective carrier lifetimes (τ_{eff}) of the L-PbS-based devices by the TPV decay, as shown in Figure 8 (c). As expected, for L-PbS QD-based devices, the variations in carrier lifetime in the high-voltage region are in line with the change in the deep defect density in the $Zn_{1-x}Mg_xO$ (x=0~0.2) films. Note that for the L-PbS QDHSCs, the τ_{eff} of devices based on x=0.15 and 0.20 are longer than that of the undoped device in the low-voltage regime, which is different from what was observed in M-PbS QDHSCs. According to the previous analysis, the medium-voltage regime is related to interfacial recombination, but the defect density of $Zn_{1-x}Mg_xO$ (x=0.15 and 0.20) is higher than that of ZnO (see Figure 7 (a)). Therefore, we confirm that the reduced charge recombination is related to the increased CBO_{spike}. In the medium-voltage regime, the value of τ_{eff} increases with increasing CBO_{spike}. However, from the photovoltaic performance of the QDHSCs based on L-PbS QDs (Figure S10), we found that the electron injection is impeded when CBO_{spike} exceeds 0.2 eV, which also results in a reduced J_{sc} and *FF*.

To investigate the role of Mg doping in electron injection from the M-PbS QDs to $Zn_{1-x}Mg_xO$ and the FTO electrode at the heterojunction, we performed femtosecond (fs)-TA spectroscopy, which has broadband capability (470~1600 nm)

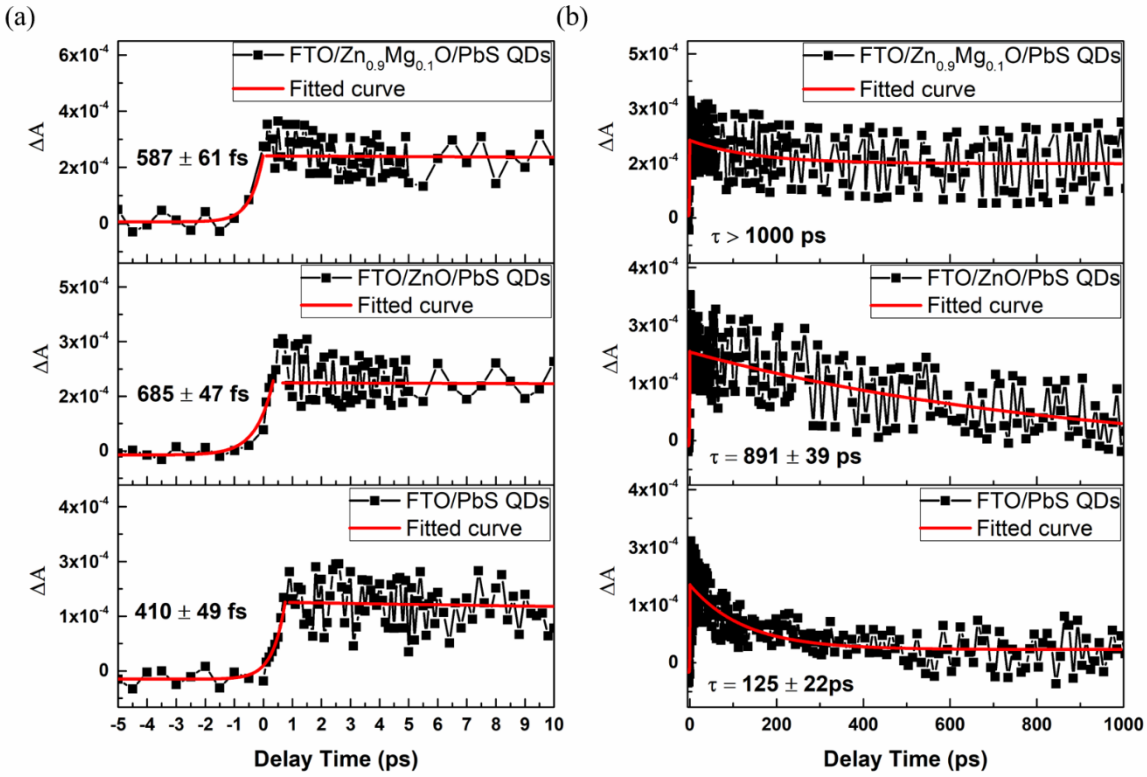

Figure 9. TA responses of the different samples of FTO/M-PbS QDs, FTO/ZnO/M-PbS QDs, and $Zn_{1-x}Mg_xO$/FTO/M-PbS QDs, measured with a pump light wavelength of 470 nm and probe wavelength of 1500 nm with a pump light intensity of 15 μJ/cm^2. (a) Injection process of the photogenerated electrons from PbS QDs into the FTO electrode (red lines are fitted lines); (b) Decay process of the injected electrons in FTO electrode (red lines are fitted lines).

and a 150 fs temporal resolution, as schematically shown in Figure S12. Because free-carrier absorption in transparent conductive glass, e.g., FTO, ZnO, and ITO, is mainly located in the infrared range (1400~4100 nm), we therefore focused on this range to investigate the dynamics of the injected electrons.[51] The dotted black line in Figure 9 shows the TA kinetics of the PbS QD layer on FTO, ZnO/FTO and $Zn_{1-x}Mg_xO$/FTO (from bottom to up). The FTO/$Zn_{1-x}Mg_xO$/PbS QD sample was excited at a wavelength of 470 nm and probed over a wavelength range of 1400 to 1600 nm, which was the same as that used for a PbS QD solution and PbS QD films deposited on glass and $Zn_{1-x}Mg_xO$ (without FTO). No TA signal was observed in this wavelength range (1400-1600 nm) for either the PbS QD solution or the PbS QD films on glass (as shown in Figure S13 (a)). In addition, no TA signal was observed for the $Zn_{1-x}Mg_xO$/PbS sample on a glass substrate (as shown in Figure S13 (b)). Therefore, we confirm that the TA response shown in Figure 9 is attributed to the absorption of electrons transferred to the FTO electrode from the PbS QDs. The TA response of the FTO/$Zn_{1-x}Mg_xO$/PbS QD composite can be well fitted using the following single exponential functions $\mathbf{y(t)} = \boldsymbol{A_0 e^{\frac{t}{\tau}} + y_0}$ (for the injection process) for time scales up to 1 ps and $\mathbf{d\,y(t)} = \boldsymbol{A_0 e^{\frac{-t}{\tau}} + y_0}$ (for the recombination process) for time scales longer than 1 ps. The bottom part of Figure 9 (a) shows the injection dynamics for photogenerated electrons transferring from the PbS QDs to FTO. The time constant (410 ± 49 fs) is much faster than that for the transfer of photoexcited electrons from PbS QDs to TiO_2 (<1 ns).[52] By introducing a ZnO thin film (~30 nm) between FTO and the PbS QD layer, the electron transfer rate decreases. We found that electron injection from the PbS QDs to the FTO electrode through the ZnO compact layer occurs on a time scale of a few hundred femtoseconds (here, 685 ± 47 fs), which is in good agreement with previous reports.[53] In addition, electron transfer from the photoexcited PbS QDs to FTO through the $Zn_{0.9}Mg_{0.1}O$ compact layer is faster (587 ± 61 fs) than that from the photoexcited PbS QDs to FTO through the ZnO compact layer. This result suggests that the photogenerated electrons are transported to the FTO electrode through the shallow defect states in $Zn_{1-x}Mg_xO$ when the CBs of $Zn_{1-x}Mg_xO$ and the QDs form a spike band structure. As seen in Figure 9 (b), the FTO/PbS QD sample shows an ultrafast recombination time of 125 ± 22 ps, but when a ZnO film was introduced between FTO and the PbS QDs, the recombination time significantly increased (895 ± 31 ps). Therefore, we conclude that the ZnO layer serves as a HBL to prevent recombination of the injected electrons in FTO with photogenerated holes in the PbS QDs, as shown in Figure S1. However, on the other hand, deep defects in ZnO can serve as recombination centres for the photogenerated electrons and holes. When $Zn_{0.9}Mg_{0.1}O$, which has fewer deep defects, was introduced as a HBL, no obvious carrier recombination was observed for up to 1 ns, which means that recombination occurs on a much longer time scale than observable by our experiments.

As shown in Figure 4 (a), the solar cells based on $Zn_{0.85}Mg_{0.15}O$ has the best PCE. According to our previous report,[9] interfacial recombination at the PbS/Au interface is important for the

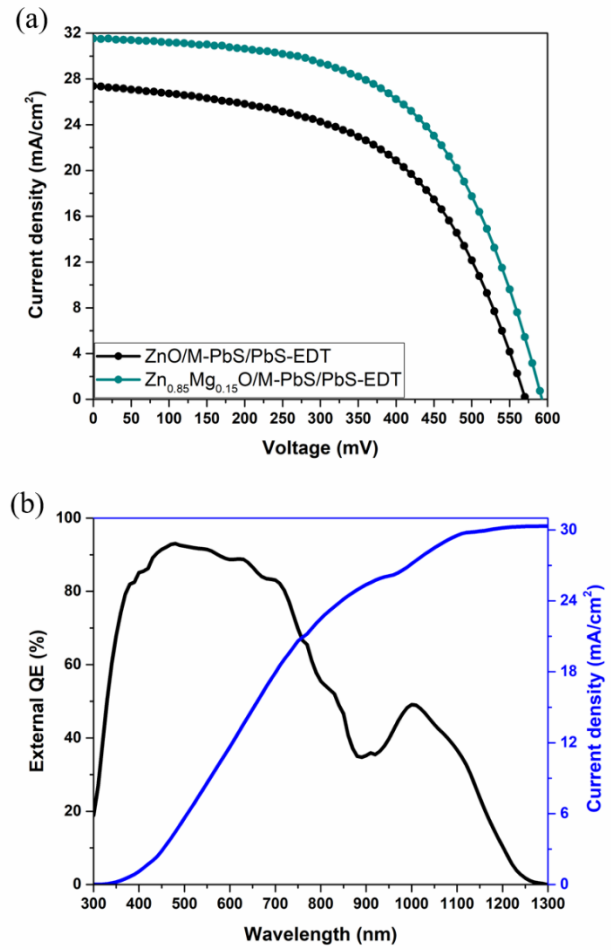

performance of QDHSCs. At present, high-efficiency PbS QDHSCs typically employ Bawendi's structure, i.e., an EDT-passivated QD layer is used as an efficient EBL (or HTL). Thus, we used Bawendi's method to introduce the EDT-treated PbS QD layer as a HTL to prevent interfacial recombination at the PbS/Au interface. We prepared five batch devices with the structure FTO/$Zn_{1-x}Mg_xO$/M-PbS (~260 nm)/PbS-EDT (~40 nm)/Au, and the J-V characteristics are shown in Figure S14 and Table S1. We found that solar cells based on $Zn_{0.85}Mg_{0.15}O$ showed the best PCE when this HTL was included. By combining all these advantages, the $Zn_{0.85}Mg_{0.15}O$/M-PbS QD-based solar cells achieved a high PCE of 10.6%, with a J_{sc} of 31.5 mA/cm^{-2} and V_{oc} of 590 mV, as shown in Figure 10 (a) and Table 4, which represents a significant improvement over the undoped device (8.3%). The external quantum efficiency (EQE) spectrum was integrated with the AM1.5 G solar spectrum of the best QDHSCs to obtain a J_{sc} of 30.3 mA/cm^2, which is in good agreement with the measured J–V result (31.52 mA/cm^2).

Figure 10. (a) *J-V* curves and (b) the external quantum efficiency of the best performing photovoltaic devices under AM 1.5G illumination. The structure of the solar cell device is FTO/$Zn_{0.85}Mg_{0.15}O$ (~30 nm)/M-PbS/EDT-PbS /Au.

Table 4. Solar cell performance obtained with $Zn_{1-x}MgxO$ (x=0, 0.15) ETLs.

Sample	J_{sc} (mA/cm^2)	V_{oc} (mV)	FF	R_s (Ω·cm^2)	R_{sh} (Ω·cm^2)	PCE (%)
x=0	27.37	571	0.534	16.18	107.57	8.35
x=0.15	31.52	590	0.570	101.46	310.91	10.60

Conclusions

In summary, for the first time, we systematically demonstrated that in QDHSCs, the formed spike structure between the ETL and QDs can inhibit charge recombination and shallow defect states in the ETL can transport photoexcited electrons from the QDs to the electron-collecting electrode. More importantly, we also revealed that this transport process occurs on the ultrafast time scale of a few hundred fs. Considering the above results, the optimized $Zn_{0.85}Mg_{0.15}O$/M-PbS QD-based device exhibited a maximum PCE of 10.6% (J_{sc} increased from 27.3 to 31.5 mA/cm^2 and V_{oc} increased from 533 to 555 mV). Our study demonstrates the importance of optimizing the energy level alignment and physical properties of the ETL layer towards the overall performance.

Corresponding Author

*Tel: 81-0424435464; e-mail: shen@pc.uec.ac.jp (Qing Shen); e-mail: hayase@life.kyutech.ac.jp (Shuzi Hayase); e-mail: minemoto@se.ritsumei.ac.jp (Takashi Minemoto); e-mail: t0b114u@cc.miyazaki-u.ac.jp (Kenji Yoshino).

Author Contributions

The manuscript was written through contributions of all authors. All authors have given approval to the final version of the manuscript.

Author Contributions

The authors declare no competing financial interest.

Acknowledgements

This research was supported by the Japan Science and Technology Agency (JST) CREST and PRESTO program and MEXT KAKENHI grant numbers 26286013 and 17H02736, and by the China Scholarship Council (CSC) of china grant number 201608050109.

Notes and references

1. S. A. McDonald, G. Konstantatos, S. Zhang, P. W. Cyr, E. J. D. Klem, L. Levina and E. H. Sargent, *Nat Mater*, 2005, **4**, 138-142.
2. P. V. Kamat, *J. Phys. Chem. C*, 2008, **112**, 18737-18753.

3. J. M. Luther, M. Law, M. C. Beard, Q. Song, M. O. Reese, R. J. Ellingson and A. J. Nozik, *Nano Lett.*, 2008, **8**, 3488-3492.
4. A. J. Nozik, M. C. Beard, J. M. Luther, M. Law, R. J. Ellingson and J. C. Johnson, *Chem. Rev.*, 2010, **110**, 6873-6890.
5. I. Kang and F. W. Wise, *Journal of the Optical Society of America B*, 1997, **14**, 1632-1646.
6. M. Liu, O. Voznyy, R. Sabatini, F. P. Garcia de Arquer, R. Munir, A. H. Balawi, X. Lan, F. Fan, G. Walters, A. R. Kirmani, S. Hoogland, F. Laquai, A. Amassian and E. H. Sargent, *Nat Mater*, 2017, **16**, 258-263.
7. J. Khan, X. Yang, K. Qiao, H. Deng, J. Zhang, Z. Liu, W. Ahmad, J. Zhang, D. Li, H. Liu, H. Song, C. Cheng and J. Tang, *Journal of Materials Chemistry A*, 2017, **5**, 17240-17247.
8. L. Hu, D.-B. Li, L. Gao, H. Tan, C. Chen, K. Li, M. Li, J.-B. Han, H. Song, H. Liu and J. Tang, *Adv. Funct. Mater.*, 2016, **26**, 1899-1907.
9. C. Ding, Y. Zhang, F. Liu, N. Nakazawa, Q. Huang, S. Hayase, Y. Ogomi, T. Toyoda, R. Wang and Q. Shen, *ACS Appl. Mater. Inter.*, 2017, DOI: 10.1021/acsami.7b06552.
10. C.-H. M. Chuang, P. R. Brown, V. Bulović and M. G. Bawendi, *Nature Materials*, 2014, **13**, 796.
11. X. Lan, S. Masala and E. H. Sargent, *Nature Materials*, 2014, **13**, 233.
12. A. G. Pattantyus-Abraham, I. J. Kramer, A. R. Barkhouse, X. Wang, G. Konstantatos, R. Debnath, L. Levina, I. Raabe, M. K. Nazeeruddin, M. Grätzel and E. H. Sargent, *ACS Nano*, 2010, **4**, 3374-3380.
13. H. Liu, J. Tang, I. J. Kramer, R. Debnath, G. I. Koleilat, X. Wang, A. Fisher, R. Li, L. Brzozowski, L. Levina and E. H. Sargent, *Adv. Mater.*, 2011, **23**, 3832-3837.
14. S. M. Willis, C. Cheng, H. E. Assender and A. A. R. Watt, *Nano Lett.*, 2012, **12**, 1522-1526.
15. W. Ke, G. Fang, J. Wan, H. Tao, Q. Liu, L. Xiong, P. Qin, J. Wang, H. Lei, G. Yang, M. Qin, X. Zhao and Y. Yan, *Nat. Commun.*, 2015, **6**, 6700.
16. J. Tang, H. Liu, D. Zhitomirsky, S. Hoogland, X. Wang, M. Furukawa, L. Levina and E. H. Sargent, *Nano Lett.*, 2012, **12**, 4889-4894.
17. I. Mora-Seró and J. Bisquert, *J. Phys. Chem. Lett.*, 2010, **1**, 3046-3052.
18. A. Braga, S. Giménez, I. Concina, A. Vomiero and I. Mora-Seró, *J. Phys. Chem. Lett.*, 2011, **2**, 454-460.
19. T. Minemoto, Y. Hashimoto, W. Shams-Kolahi, T. Satoh, T. Negami, H. Takakura and Y. Hamakawa, *Sol. Energy Mater. Sol. Cells*, 2003, **75**, 121-126.
20. R. L. Z. Hoye, B. Ehrler, M. L. Böhm, D. Muñoz-Rojas, R. M. Altamimi, A. Y. Alyamani, Y. Vaynzof, A. Sadhanala, G. Ercolano, N. C. Greenham, R. H. Friend, J. L. MacManus-Driscoll and K. P. Musselman, *Adv. Energy Mater.*, 2014, **4**, 1301544-n/a.
21. X. Zhang and E. M. J. Johansson, *Journal of Materials Chemistry A*, 2017, **5**, 303-310.
22. D. C. Olson, S. E. Shaheen, M. S. White, W. J. Mitchell, M. F. A. M. van Hest, R. T. Collins and D. S. Ginley, *Adv. Funct. Mater.*, 2007, **17**, 264-269.
23. Z. Yin, Q. Zheng, S.-C. Chen and D. Cai, *ACS Appl. Mater. Inter.*, 2013, **5**, 9015-9025.
24. C. J. Raj, K. Prabakar, S. N. Karthick, K. V. Hemalatha, M.-K. Son and H.-J. Kim, *J. Phys. Chem. C*, 2013, **117**, 2600-2607.
25. S. Bang, S. Lee, Y. Ko, J. Park, S. Shin, H. Seo and H. Jeon, *Nanoscale Research Letters*, 2012, **7**, 290.
26. S.-H. Liao, H.-J. Jhuo, Y.-S. Cheng and S.-A. Chen, *Adv. Mater.*, 2013, **25**, 4766-4771.
27. T. Yang, W. Cai, D. Qin, E. Wang, L. Lan, X. Gong, J. Peng and Y. Cao, *J. Phys. Chem. C*, 2010, **114**, 6849-6853.
28. Z. Yin, Q. Zheng, S.-C. Chen, D. Cai, L. Zhou and J. Zhang, *Adv. Energy Mater.*, 2014, **4**, 1301404-n/a.
29. M. Wei, R. C. Boutwell, J. W. Mares, A. Scheurer and W. V. Schoenfeld, *Appl. Phys. Lett.*, 2011, **98**, 261913.
30. J. Tauc, R. Grigorovici and A. Vancu, *physica status solidi (b)*, 1966, **15**, 627-637.
31. H. H. Zhang, X. H. Pan, B. Lu, J. Y. Huang, P. Ding, W. Chen, H. P. He, J. G. Lu, S. S. Chen and Z. Z. Ye, *Phys. Chem. Chem. Phys.*, 2013, **15**, 11231-11235.
32. T. Minemoto, Y. Hashimoto, T. Satoh, T. Negami, H. Takakura and Y. Hamakawa, *J. Appl. Phys.*, 2001, **89**, 8327-8330.
33. J. Tang, K. W. Kemp, S. Hoogland, K. S. Jeong, H. Liu, L. Levina, M. Furukawa, X. Wang, R. Debnath, D. Cha, K. W. Chou, A. Fischer, A. Amassian, J. B. Asbury and E. H. Sargent, *Nat Mater*, 2011, **10**, 765-771.
34. T. Törndahl, C. Platzer-Björkman, J. Kessler and M. Edoff, *Progress in Photovoltaics: Research and Applications*, 2007, **15**, 225-235.
35. T. Minemoto and M. Murata, *Sol. Energy Mater. Sol. Cells*, 2015, **133**, 8-14.
36. R. B. M. Cross, M. M. D. Souza and E. M. S. Narayanan, *Nanotechnology*, 2005, **16**, 2188.
37. S. Vempati, J. Mitra and P. Dawson, *Nanoscale Research Letters*, 2012, **7**, 470.
38. K. Tvrdy, P. A. Frantsuzov and P. V. Kamat, *Proc. Natl. Acad. Sci. U. S. A.*, 2011, **108**, 29-34.
39. B.-R. Hyun, A. C. Bartnik, L. Sun, T. Hanrath and F. W. Wise, *Nano Lett.*, 2011, **11**, 2126-2132.
40. P. Tiwana, P. Docampo, M. B. Johnston, L. M. Herz and H. J. Snaith, *Energy & Environmental Science*, 2012, **5**, 9566-9573.
41. B. Ehrler, K. P. Musselman, M. L. Böhm, F. S. F. Morgenstern, Y. Vaynzof, B. J. Walker, J. L. MacManus-Driscoll and N. C. Greenham, *ACS Nano*, 2013, **7**, 4210-4220.
42. K. K. N. Simon M. Sze, *Physics of Semiconductor Devices*, Wiley-Interscience, New York, USA, 3rd Edition edn., 2006.
43. J. D. Servaites, M. A. Ratner and T. J. Marks, *Energy & Environmental Science*, 2011, **4**, 4410-4422.
44. H. Saitoh, A. Takano, S. Kawaguchi, T. Washio, S. Ohshio and H. Akasaka, *J. Ceram. Soc. Jpn.*, 2009, **117**, 780-782.
45. X. Zhang, D. Yang, Z. Yang, X. Guo, B. Liu, X. Ren and S. Liu, *Sci. Rep.*, 2016, **6**, 35091.
46. J. Chang, Y. Kuga, I. Mora-Sero, T. Toyoda, Y. Ogomi, S. Hayase, J. Bisquert and Q. Shen, *Nanoscale*, 2015, **7**, 5446-5456.
47. Y. Zhang, C. Ding, G. Wu, N. Nakazawa, J. Chang, Y. Ogomi, T. Toyoda, S. Hayase, K. Katayama and Q. Shen, *J. Phys. Chem. C*, 2016, **120**, 28509-28518.
48. Y. Zhang, G. Wu, I. Mora-Seró, C. Ding, F. Liu, Q. Huang, Y. Ogomi, S. Hayase, T. Toyoda, R. Wang, J. Otsuki and Q. Shen, *J. Phys. Chem. Lett.*, 2017, **8**, 2163-2169.
49. C.-H. M. Chuang, A. Maurano, R. E. Brandt, G. W. Hwang, J. Jean, T. Buonassisi, V. Bulović and M. G. Bawendi, *Nano Lett.*, 2015, **15**, 3286-3294.
50. D. Bozyigit, S. Volk, O. Yarema and V. Wood, *Nano Lett.*, 2013, **13**, 5284-5288.

51. T. Minami, in *Semiconductors and Semimetals*, eds. B. G. Svensson, S. J. Pearton and C. Jagadish, Elsevier, 2013, vol. 88, pp. 159-200.
52. H. C. Leventis, F. O'Mahony, J. Akhtar, M. Afzaal, P. O'Brien and S. A. Haque, *J. Am. Chem. Soc.*, 2010, **132**, 2743-2750.
53. M. Eita, A. Usman, A. a. O. El-Ballouli, E. Alarousu, O. M. Bakr and O. F. Mohammed, *Small*, 2015, **11**, 112-118.